

A multicomponent coupled model of glacier hydrology 2. Application to Trapridge Glacier, Yukon, Canada

Gwenn E. Flowers and Garry K. C. Clarke

Department of Earth and Ocean Sciences, University of British Columbia, Vancouver, British Columbia, Canada

Received 30 August 2001; revised 9 March 2002; accepted 14 March 2002; published 12 November 2002.

[1] A new glaciohydraulic model is tailored to Trapridge Glacier, Yukon, Canada, where long-term measurements of subglacial water pressure provide parameter constraints and a platform for model evaluation. Using digital elevation models and meteorological data as input, we investigate hydrology on diurnal and seasonal timescales. Quantitative comparisons of simulated and observed pressure records allow us to select a reference model objectively, from which we gain first insights into the gross spatial characteristics of the drainage system. Equilibrium simulations highlight target areas for water storage and potential sticky spots, both of which have established relevance to glacier dynamics. Seasonal simulations capture the key signatures of spring and autumn transitions and corroborate our understanding of the processes involved. Successfully modeled features of the spring transition include increased hydraulic coupling between the surface and bed with time, temporary augmentation of subglacial storage, and rapid subglacial transitions from a hydraulically unconnected to connected state. Autumn transitions are characterized by deterioration of the basal drainage network, drawdown of subglacial storage reservoirs, and heightened sensitivity to precipitation and surface refreezing. Finally, we draw attention to the important role of groundwater transport in cold glacial environments where permafrost can impede drainage from the ice margin. *INDEX TERMS:* 1827 Hydrology: Glaciology (1863); 1863 Hydrology: Snow and ice (1827); 9315 Information Related to Geographic Region: Arctic region; *KEYWORDS:* subglacial hydrology, glacier runoff, glaciohydraulic modeling, Trapridge Glacier, water pressure, permafrost

Citation: Flowers, G. E., and G. K. C. Clarke, A multicomponent coupled model of glacier hydrology, 2, Application to Trapridge Glacier, Yukon, Canada, *J. Geophys. Res.*, 107(B11), 2288, doi:10.1029/2001JB001124, 2002.

1. Introduction

[2] Links between glacier hydraulics and dynamics have been deciphered from a combination of theory [e.g., *Kamb*, 1970; *Iken*, 1981; *Bindschadler*, 1983; *Fowler*, 1987; *Alley*, 1989] and observation [e.g., *Iken et al.*, 1983; *Iken and Bindschadler*, 1986; *Fischer and Clarke*, 1997; *Harbor et al.*, 1997; *Björnsson*, 1998] and continue to inspire new developments in glaciohydraulic modeling [e.g., *Arnold et al.*, 1998]. In this paper, we apply the multicomponent model outlined by *Flowers and Clarke* [2002] to a surge-type glacier.

[3] Our purpose is threefold: (1) to evaluate the veracity of the model by comparing simulated subglacial records with field data, (2) to provide a preliminary basin-scale context for study-site measurements, and (3) to understand the spatial and temporal drainage system evolution that gives rise to seasonal variability in basal water pressure measurements. We use existing digital elevation models (DEMs) as geometric input and force the surface model with observed meteorological quantities. Subglacial measurements provide objective constraints on model parameters. Seasonal transitions form an illuminating case study

because they involve the development and collapse of various drainage modes, and they illustrate interactions between basal hydraulics and mechanics.

[4] Our study site, Trapridge Glacier, is a ~4-km-long outlet glacier, located on the eastern flank of Mount Wood (latitude 61°14'N, longitude 140°20'W) in Kluane Park Reserve, Yukon, Canada (Figure 1a). It spans an elevation range of ~2250–2800 m above sea level (asl) [*Stone*, 1993], and the mean ice thickness is 70 m over the lowermost 2.5 km of the glacier. Sometime during the 1940s Trapridge experienced a rapid advance (“surge”) and has since undergone dramatic thermal and geometrical evolution back to its presurge state [*Clarke and Blake*, 1991]. The ice is polythermal, hence below the melting point (-7° at 15 m depth) except near the glacier bed.

[5] In the study area (2360 m asl), where the ice is 60–70 m thick, the mean annual glacier surface velocity is ~ 30 m yr⁻¹. At least ~90% of this motion is accounted for by a combination of sliding and bed deformation [*Blake*, 1992]. A layer of deformable saturated sediment, 0.3–0.5 m thick, underlies the ice in this area [*Blake*, 1992]. Sedimentary studies in the Trapridge Glacier forefield reveal transmissive layers of sand and gravel totalling a few meters in thickness, with hydraulic conductivities between 10^{-5} and 10^{-3} m s⁻¹ [*Stone*, 1993]. These units are capped by

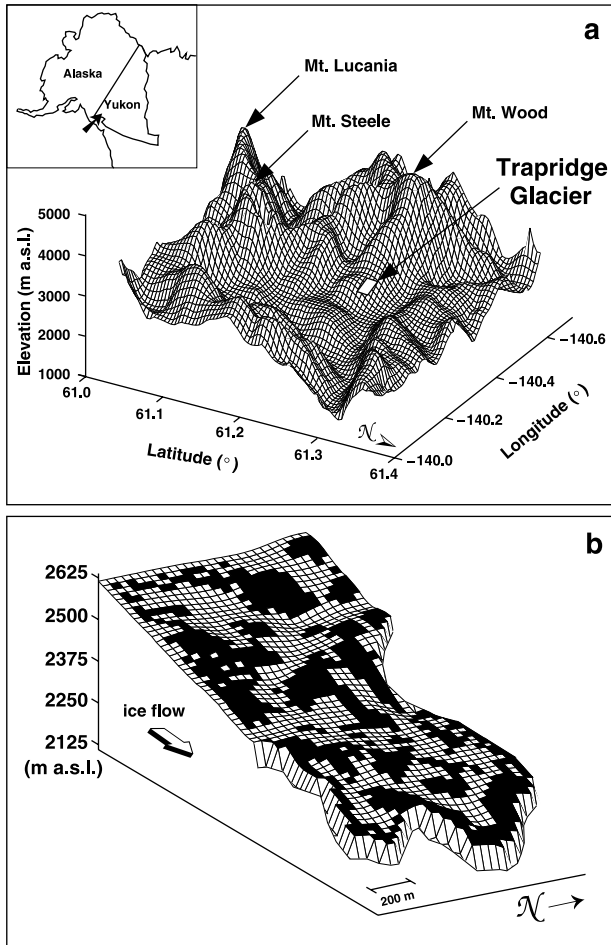


Figure 1. Digital models of Trapridge Glacier and its surroundings. (a) Trapridge Glacier location. Topography is interpolated from a $400 \text{ m} \times 400 \text{ m}$ digital elevation model provided by the Geological Survey of Canada and Parks Canada. (b) Digital representation of crevasse distribution superimposed on the ice surface DEM. Shaded cells contain crevasses.

decimeters to a meter of till with conductivities in the range 10^{-12} - 10^{-7} m s^{-1} [Stone, 1993].

[6] Over the last 15 years, spatially dense instrumentation of the glacier bed has significantly improved our understanding of subglacial hydrology and basal mechanics [e.g., Clarke, 1987; Blake et al., 1994; Fischer and Clarke, 1994; Murray and Clarke, 1995; Stone and Clarke, 1996; Kavanaugh and Clarke, 2001]. Subglacial water pressure sensors, emplaced in boreholes, often record large diurnal fluctuations during the summer in response to the influx of surface meltwater. In winter, records from different instruments are generally uncorrelated. Sediments are frozen near the glacier margin and no visible hydraulic outlets (e.g., channels) develop. Except during extreme events, when floodwaters breach the thermal dam, subglacial water escapes through subsurface aquifers [Stone, 1993; Flowers and Clarke, 2000]. Long-term, in situ observations of subglacial dynamics render Trapridge excellent for relating basin-scale hydrology to process-scale subglacial phenomena.

2. Theory

[7] Four time-dependent equations form the skeleton of the multicomponent hydrology model detailed by Flowers and Clarke [2002]. Each equation describes the vertically integrated water balance in one of four coupled systems: surface runoff (r), englacial storage and transport (e), subglacial (basal) drainage (s), and flow in a subsurface aquifer (a). In order, these equations are

Surface

$$\frac{\partial h^r}{\partial t} + \frac{\partial Q_j^r}{\partial x_j} = M + R - \phi^{r:e} + \phi^{r:s} - \phi^{r:a} \quad (1)$$

Englacial

$$\frac{\partial h^e}{\partial t} + \frac{\partial Q_j^e}{\partial x_j} = \phi^{r:e} - \phi^{e:s} \quad (2)$$

Subglacial

$$\frac{\partial h^s}{\partial t} + \frac{\partial Q_j^s}{\partial x_j} = b^s - \phi^{r:s} + \phi^{e:s} - \phi^{s:a} \quad (3)$$

Aquifer

$$\left(\frac{h^a}{\rho^a}\right) \frac{\partial p^a}{\partial t} + \frac{\partial h^a}{\partial t} + \frac{\partial Q_j^a}{\partial x_j} = \phi^{s:a} + \phi^{r:a} \quad (4)$$

where t is time and x_j is the two-dimensional horizontal spatial coordinate. Dependent variables $h^r(x, y, t)$, $h^e(x, y, t)$, $h^s(x, y, t)$, and $h^a(x, y, t)$ are the local water thicknesses in each system. Fluid density $\rho^a = \rho_w \exp(\beta p^a)$ with $\rho_w = 1000 \text{ kg m}^{-3}$, $\beta = 5.04 \times 10^{-10} \text{ Pa}^{-1}$, and p^a the fluid pressure above a datum $p_0 \approx 0$. Variables $Q_j^r(x, y, t)$, $Q_j^e(x, y, t)$, $Q_j^s(x, y, t)$, and $Q_j^a(x, y, t)$ are horizontal fluid fluxes.

[8] Water sources, sinks, and production appear on the right-hand sides of equations (1)–(4). Quantities M , R , and b^s represent rates of surface ablation, rainfall, and production of basal water, respectively. Intercomponent water exchange terms $\phi^{r:e}(x, y, t)$, $\phi^{r:s}(x, y, t)$, $\phi^{r:a}(x, y, t)$, $\phi^{e:s}(x, y, t)$, and $\phi^{s:a}(x, y, t)$ depend on fluid potential differences between adjacent systems, and thereby provide mathematical coupling.

[9] Ablation and precipitation drive the surface model, and the resulting supraglacial runoff flows over and off the glacier, or to the bed through a system of crevasses, pipes, and fractures (Figure 1b). Basal water is transported in a macroporous sediment horizon where it may also infiltrate the underlying groundwater aquifer. Although subglacial drainage is treated as porous sheet flow, it is distinguished from flow in a traditional aquifer by nonlinear parameterizations of hydraulic conductivity and water pressure as a function of water sheet thickness h^s . The reader is referred to Flowers and Clarke [2002] for ancillary equations and further explanation of the theory.

2.1. Surface Hydrology

[10] To calculate ablation, we adopt Hock's [1999] spatially distributed temperature index method which includes the effects of potential direct solar radiation. The melt rate M of snow or ice is expressed as

$$M = \begin{cases} T (MF + a_{\text{snow/ice}} I) & T > 0 \\ 0 & T \leq 0, \end{cases} \quad (5)$$

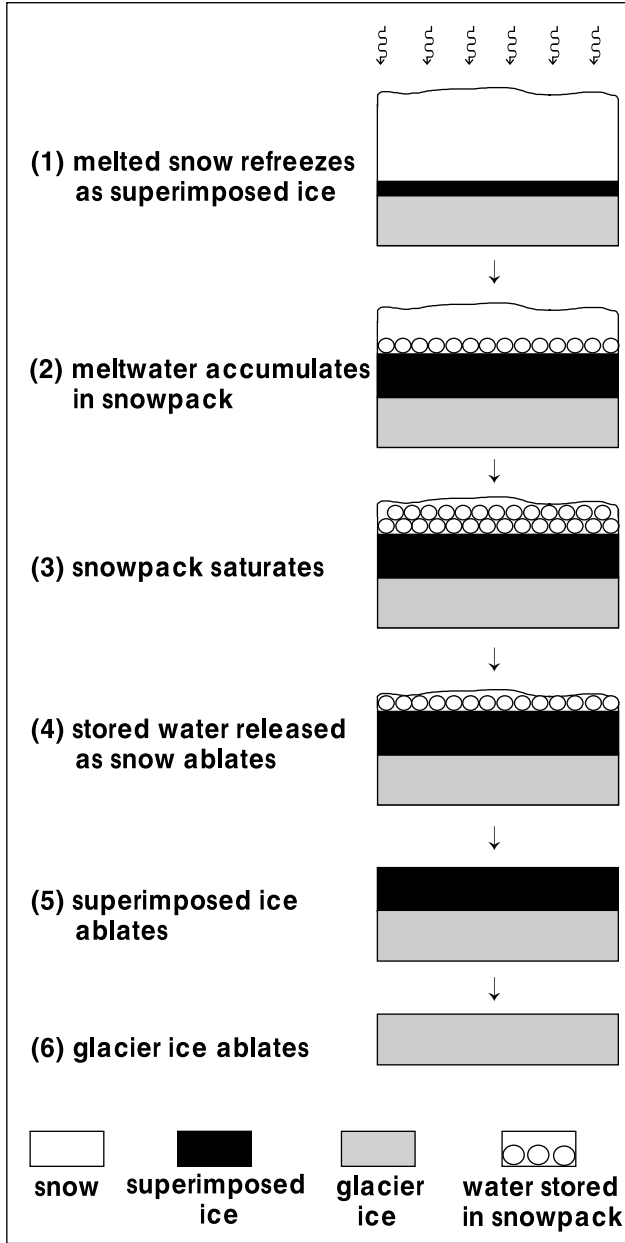


Figure 2. Ablation stages represented in the surface model.

where T is air temperature, MF and $a_{\text{snow/ice}}$ are melt and radiation factors, respectively, and I is potential direct solar radiation. Melt and radiation factors are assumed to be uniform in space and time. *Hock* [1999] computes radiation as

$$I = I_0 \left(\frac{R_m}{R} \right)^2 \psi_a \left(\frac{P}{P_0 \cos Z} \right) \cos \theta, \quad (6)$$

with solar constant $I_0 = 1368 \text{ W m}^{-2}$ [Fröhlich, 1993], R_m/R the mean over instantaneous Sun-Earth distance, clear-sky transmissivity $\psi_a = 0.75$, P/P_0 the atmospheric pressure relative to sea level, Z the local zenith angle, and θ the solar incidence angle. Incidence angle is computed as a function of slope, aspect, solar azimuth, and zenith angle [Garnier and Ohmura, 1968]. Radiation is set to zero during times when the

surrounding terrain casts a shadow on the glacier surface. To compute ablation using this method requires a DEM of the glacier and its surroundings, parameters MF , a_{snow} , and a_{ice} , a time series of air temperature at a known elevation, and a value for the surface lapse rate.

[11] As shown in Figure 2, modeled snowmelt refreezes as superimposed ice [Reeh, 1991]. This is presumed to occur instantaneously and accounts for some lost energy by requiring the first portion of the snowpack to be melted twice. The same radiation factor a_{ice} is used for superimposed and glacier ice. When superimposed ice comprises a certain water-equivalent fraction of the original snowpack (PMAX), refreezing stops and subsequent melt is stored as liquid within the snow.

[12] Although $\text{PMAX} = 0.6$ is usually taken as constant [Reeh, 1991], we follow a different approach. On the premise that the maximum thickness of superimposed ice $D_{\text{ice}}^{\text{max}}$ is determined by the near-surface glacier temperature (assumed to be equal to the mean annual air temperature, MAAT) [Ward and Orvig, 1953], Woodward *et al.* [1997] derive the empirical relationship

$$D_{\text{ice}}^{\text{max}} = -0.69 \times \text{MAAT} + 0.0096 \quad (7)$$

for $D_{\text{ice}}^{\text{max}}$ in centimeters and MAAT in $^{\circ}\text{C}$. PMAX is then calculated as $D_{\text{ice}}^{\text{max}}/D_{\text{snow}}^0$ where D_{snow}^0 is the water-equivalent depth of snow in centimeters at the beginning of the melt season.

[13] Modeled surface runoff begins when the snowpack saturates, and water is released from storage with further ablation of the snow. We assume that water is uniformly distributed within the saturated snow column, so the amount of water released depends only on snowpack porosity. Because we do not physically model water transport within the snowpack, there is no horizontal transport of snowmelt prior to its release. Where snow is present in the model, it retards meltwater delivery to the glacier interior as parameterized by

$$\phi^{r:e}(s) = \phi^{r:e}(0) \exp(-s/s_c), \quad (8)$$

where $\phi^{r:e}(0)$ is the rate of water exchange in the absence of snow, s is the areally averaged water-equivalent snow depth, and s_c is a critical depth required to reduce the exchange by $1/e$.

2.2. Numerical Method

[14] Equations (1)–(4) are discretized on a staggered Cartesian grid using second-order finite difference approximations. We obtain simultaneous solutions to the coupled system using a Newton-Krylov iterative procedure. The surface runoff component is solved explicitly, while the remaining components are solved semi-implicitly (Crank-Nicolson). Numerical parameters are listed in Table 1. A thorough description of the model numerics is given by Flowers [2000].

3. Model Inputs

3.1. Glacier Geometry and Climate Forcing

[15] DEMs of the glacier surface and bed (pixel size $40 \times 40 \text{ m}$), derived from optical and radio echo surveys [Flowers and Clarke, 1999], form the geometric platform for this investigation. We construct a digital representation of the

Table 1. Physical Constants and Numerical Model Parameters

Parameter	Value	Definition
Physical constants		
ρ_w	1000 kg m ⁻³	density of water at 0°C
ρ_i	910 kg m ⁻³	density of ice
g	9.81 m s ⁻²	gravitational acceleration
β	5.04×10^{-10} Pa ⁻¹	compressibility of water
Numerical parameters		
L_x	2560 m	model domain, longitudinal
L_y	1120 m	model domain, transverse
n_x	64	number of grid cells in x
n_y	28	number of grid cells in y
Δx	40 m	longitudinal grid spacing
Δy	40 m	transverse grid spacing
Δt	120–300 s	maximum time step

crevasse distribution (Figure 1b) by using convexity of the ice surface DEM as a proxy for strain, and thus a reasonable indicator of crevasse habitat. Results of this method are verified by comparison with aerial photographs. To calculate potential direct solar radiation for the ablation model, we use a DEM of the glacier surroundings (pixel size 400×400 m) prepared by the Geological Survey of Canada (GSC), in cooperation with Parks Canada. This DEM includes the skyline as perceived from any point on the glacier. To splice the glacier- and regional-scale data sets, we interpolate the latter onto a 40-m grid and insert the radar-derived DEM for the glacier. Uncertainty in the rendering of surrounding terrain is unimportant, as long as the skyline is accurately portrayed. Using this composite DEM, digital models of slope, aspect, and radiation are computed.

[16] All models are driven with air temperature time series recorded by data loggers operating year-round on Trapridge Glacier. In the absence of mass balance or basin discharge measurements, it is impossible to calibrate parameters MF and $a_{\text{snow/ice}}$ rigorously. Rather, using 1997 temperature data from the study area, we scale MF and $a_{\text{snow/ice}}$ as given by *Hock* [1999] to produce approximately 1 m of ablated ice (assuming $\rho_i = 910 \text{ kg m}^{-3}$) as observed from days 184–207. Constraining ablation in this way yields a scaling factor for the melt parameters of 0.667.

3.2. Boundary Conditions

[17] As described by *Flowers and Clarke* [2002], surface runoff is collected in a potential trough at the edge of the model domain. No flow is permitted in the trough, such that water collection remains unaffected by arbitrary Dirichlet boundary conditions. No-flow conditions are imposed on both the englacial and subglacial systems where ice intersects the grid edge. Because our model grid encompasses all of the glacier ablation area and much of its accumulation area, no-flow conditions are probably a reasonable approximation to reality. Dirichlet conditions are imposed at the glacier margin: $p^e = p^s = 0|_{h_f=0}$. No-flow conditions are imposed at the upstream boundary of the aquifer, and Dirichlet conditions along the remainder of the rectangular grid edge. Along the lateral boundaries $h^a = n^a d^a$ and downstream $h^a = 0.9 n^a d^a$.

4. Choosing a Reference Model

[18] Quantitative comparisons between model results and basal water pressure records from Trapridge Glacier permit

an objectively guided parameter selection. We aim to identify a preferred parameter set, or reference model, with which to conduct both steady state and time-dependent investigations. A dense array of subglacial pressure transducers that was deployed in 1997 (Figure 3a) produced exceptionally coherent records, as shown for days 190–204 (9–23 July) in Figure 3b. Pulses of surface meltwater produce the dominant diurnal fluctuations with amplitudes of 10–25 m about a mean of 45 m (78% flotation). The

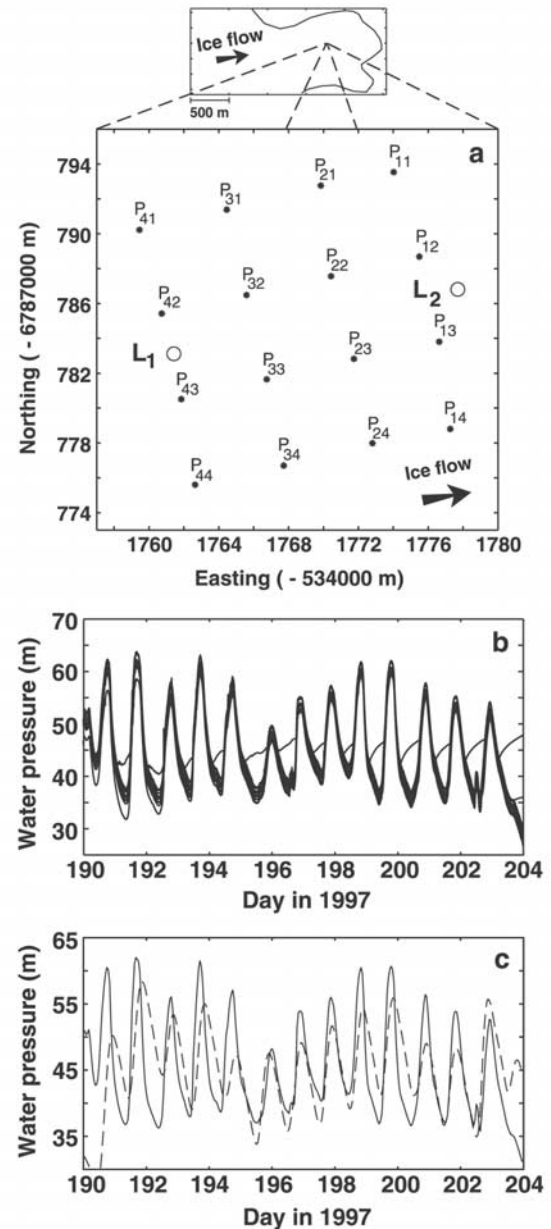


Figure 3. Data source for model parameter optimization. (a) Dense array of pressure transducers beneath Trapridge Glacier. Dots indicate instrument borehole locations and open circles mark data loggers. (b) Subglacial water pressure as recorded by sensors labeled in Figure 3a for days 190–204, 1997. (c) Comparison of observations (solid line) and reference model simulation (dashed line).

Table 2. Reference Model Parameters for Trapridge Glacier^a

Parameter	Value	Definition	Source
Ablation/runoff			
MF	$1.39 \times 10^{-8} \text{ m s}^{-1} \text{ }^\circ\text{C}^{-1}$	melt factor	S
a_{snow}	$1.11 \times 10^{-10} \text{ m}^2 \text{ W}^{-1} \text{ m s}^{-1} \text{ }^\circ\text{C}^{-1}$	radiation factor, snow	S
a_{ice}	$1.47 \times 10^{-10} \text{ m}^2 \text{ W}^{-1} \text{ m s}^{-1} \text{ }^\circ\text{C}^{-1}$	radiation factor, ice	S
ρ_{snow}	92.0 kg m^{-3}	snow density	F
n_{snow}	0.15	snowpack porosity	F
LR	$0.0065^\circ\text{C m}^{-1}$	atmospheric lapse rate	F
K^r	0.2 m s^{-1}	effective hydraulic conductivity	C
$\tau^{r:e}$	120 s	time constant for water exchange	C
s_c	0.1 m w.e.	critical snow depth, equation (8)	F
$\chi^{r:e}$	1	runoff-englacial coupling strength	F
$\chi^{r:a}$	1	runoff-groundwater coupling strength	F
Englacial storage/transport			
V_T/V_I	1×10^{-4}	maximum storage volume fraction	C
γ_1	0	relative abundance of moulins	F
γ_2	1	relative abundance of surface crevasses	F
γ_3	0	relative abundance of basal crevasses	F
f_2	0	crevasse tapering factor	C
K^e	$1.0 \times 10^{-9} \text{ m s}^{-1}$	englacial hydraulic conductivity	F
$\tau^{e:s}$	7200 s	time constant for water exchange	F
$\chi^{e:s}$	0.1	englacial-subglacial coupling strength	F
Subglacial sediment sheet			
h_c^s	0.15 m	critical sheet water thickness	D
K_{min}^s	$2.5 \times 10^{-2} \text{ m s}^{-1}$	minimum hydraulic conductivity	C
K_{max}^s	$5.0 \times 10^{-2} \text{ m s}^{-1}$	maximum hydraulic conductivity	C
k_a	15	scaling parameter	D
k_b	0.85	scaling parameter	D
K_f	$1.0 \times 10^{-10} \text{ m s}^{-1}$	hydraulic conductivity of frozen soil	C
v	30 m yr^{-1}	average glacier sliding velocity	Kavanaugh [2000]
$\chi^{s:a}$	1	subglacial-aquifer coupling strength	F
Till cap properties			
d^t	1.0 m	thickness	Stone [1993]
K^t	$5.0 \times 10^{-8} \text{ m s}^{-1}$	hydraulic conductivity	C
Groundwater aquifer			
d^a	3.0 m	thickness	Stone [1993]
K^a	$4.0 \times 10^{-4} \text{ m s}^{-1}$	hydraulic conductivity	C
n^a	0.4	porosity	Freeze and Cherry [1979]
α	$1.0 \times 10^{-8} \text{ Pa}^{-1}$	compressibility	Freeze and Cherry [1979]

^a Some quantities apply to equations of *Flowers and Clarke* [2002]. Source key is as follows: S, scaled from value given by *Hock* [1999]; C, determined from sensitivity tests and comparison with field records [*Flowers*, 2000]; F, fixed value; D, derived independently by *Flowers* [2000].

behavior of the visible outlier (sensor P₄₂) in Figure 3b is indicative of a diurnally enabled hydraulic connection [*Murray and Clarke*, 1995].

[19] To facilitate comparison between simulated and observed records, we average the traces in Figure 3b into a single master time series. Model results from the overlapping grid cell are then compared directly to the data. Thirty-three diagnostic tests were performed, varying seven parameters independently and in combination. Tests were initiated with a prescribed constant surface melt rate of $3.5 \times 10^{-7} \text{ m water equivalent (w.e.) s}^{-1}$ ($\sim 3 \text{ cm w.e. d}^{-1}$) and run to equilibrium before introducing a time-dependent surface forcing. For 6 days before the comparison interval (day 190–204) the model was driven by a temperature time series from data logger L₁ (Figure 3a). Precipitation was negligible during this period. To quantitatively discriminate between our test simulations, we compute the difference between simulated and observed records with respect to (1) mean water pressure, (2) oscillation amplitude, and (3) oscillation phase. As our reference model, we choose the one that minimizes a weighted combination of these three differences. Reference parameters are listed in Table 2, and the resulting simulated time series plotted in Figure 3c.

[20] In addition to enabling parameter refinement, these tests demonstrate that the basic model successfully emulates

typical melt season behavior. The mean subglacial water pressure predicted by the model is within 0.25 m of the observed value. Due to the presence of a frozen glacier margin, this quantity is largely a function of subsurface conductivities (K^t , K^a) in the model. The most noteworthy differences between observed and simulated records lie in the amplitude and phase of diurnal oscillations. More subtle differences lie in the value of daily pressure minima and in the shape of the cycles.

[21] Amplitudes are generally underestimated by the model, pointing to one of the shortcomings of our simple continuum approach. In reality, heterogeneity in the subglacial environment confines drainage to some fraction of the glacier bed, resulting in higher peak pressures than are expected for a uniformly distributed fluid. *Kavanaugh and Clarke* [2001] have noted that periods of high meltwater flux to the glacier bed tend to increase basal drainage capacity, resulting in a depression of measured water pressure minima. Although simulated pressure minima are occasionally lower than those observed (Figure 3c), we would not generally expect to capture the depth of all diurnal pressure cycles without allowing for dynamic adjustments in subglacial drainage system volume. Channelization of supraglacial runoff, also neglected in the model, may be an additional source of discrepancy between simu-

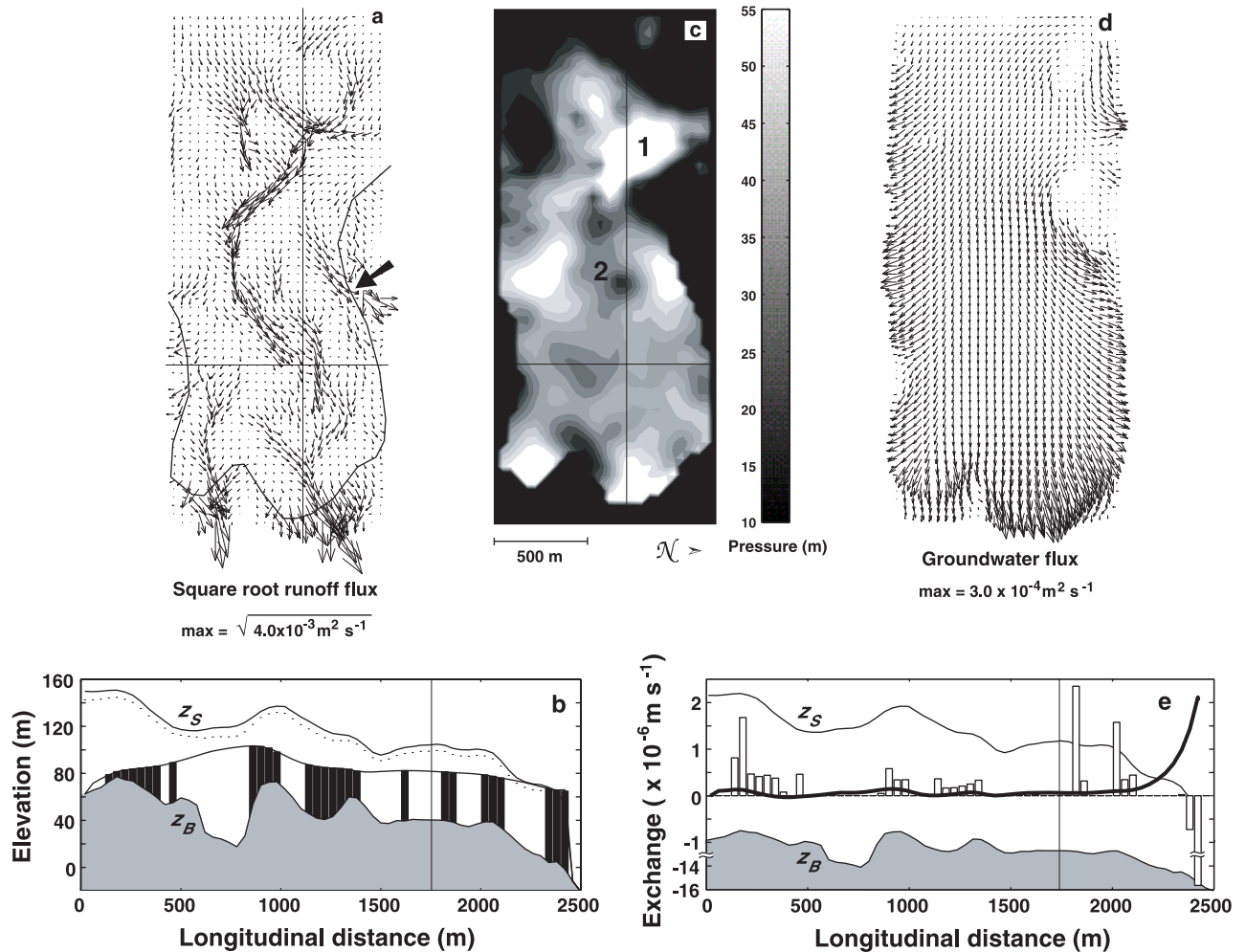


Figure 4. Trapridge Glacier reference model equilibrium. (a) Surface water flow field shown as the square root of runoff flux. Crosshairs intersect the study area and test point. Arrow indicates the origin of an ice marginal stream. (b) Longitudinal profiles of englacially stored water (bars) and subglacial hydraulic head (line) shown with ice surface and bed topography. Flotation level is indicated by the dotted line. All profiles are plotted with a 7° slope removed and an arbitrary elevation datum. Profile location is shown in Figure 4a, and the vertical line is centered on the study area. (c) Subglacial water pressure expressed in meters. (d) Groundwater flow vectors. (e) Longitudinal profiles of $\phi^{e:s}$ (vertical bars) and $\phi^{s:a}$ (line).

lated and observed fluctuations, especially where channels are misaligned with the grid-scale surface slope.

[22] Phase mismatch between simulated and observed records is most conspicuous before day 196. The integrity of our derived crevasse map in representing the actual entry portals for surface water bears on this issue, as does the model assumption that horizontal transport of meltwater within the glacier body is minimal. Both factors may contribute to errors in phase by misrepresenting the travel distance of meltwater from its origin to the instrument study area at the bed.

[23] Daily pressure maxima occur between 2100 and 2400 hours in the simulation, as compared to 1600–2400 hours in the observations. Variations in the time of daily maximum track each other in the two records after day 196. Because the model neglects ice and bed mechanics, it produces a relatively simple convolution of the surface forcing in the basal pressure response. Therefore the similarity in phase evolution between observations and simulations after day 196 marks a simplification in the real-system response to surface

air temperature. It snowed several times in the days prior to 190, possibly resulting in a volume reduction of the active drainage network. This is consistent with the observed prematurity of daily pressure maxima during days 191–195. High melt rates were calculated on four days between days 190 and 195, with day 195 being the highest. This presumably resulted in an enlargement of the drainage system. Given the limitations imposed by neglecting ice dynamics and bed thermal conditions, we consider the correspondence between modeled and observed records in Figure 3c to be very good.

5. Steady State Simulations

[24] Using the reference parameters in Table 2, we run the model to equilibrium. Figure 4 summarizes the salient features of the resulting reference model hydrology. Simulated supraglacial meltwater is transported in several channels through crevasse-free areas, and drainage paths

converge near the terminus where waterfalls are observed in the field during the melt season (Figure 4a). The model also predicts runoff from the northern side of the glacier (arrow, Figure 4a) where an ice marginal stream is known to originate. The simulated concentration of surface flow through the study area can be qualitatively verified by the nearby development of observed supraglacial swamps.

[25] Figure 4b shows modeled englacial storage along a profile intersecting the study area. Though crevasses are sparsely distributed along the profile, storage levels give a reasonable indication of the predicted structure of the subglacial hydraulic head (dashed line, Figure 4b). The simulated water table meets the glacier surface approximately 100 m from the terminus, where artesian water pressures have occasionally produced observed eruptions of subglacial water.

[26] Steady state subglacial water pressure is shown in Figure 4c. The frozen glacier margin produces distinctively high pressures at the terminus. Other high-pressure (bright) areas in Figure 4c are related to bedrock depressions, for example, between 600 and 800 m from the head of the glacier (label 1). Bedrock protuberances prevent water accumulation, producing local minima in the water distribution (and hence pressure field in this case) as can be seen directly west of the study site (Figure 4c, label 2). These unlubricated areas or “sticky” spots play a key role in balancing glacier driving stress [e.g., Fischer and Clarke, 1997]. Hydromechanical destabilization of these glacier pinning points can lead to unsteady flow, and has been used to explain unusual subglacial events recorded by sensors in the study area [Kavanaugh and Clarke, 2001].

[27] Beneath the glacier, simulated aquifer saturation (not shown) mirrors basal water pressure. This is a combined result of aquifer topography (assumed to be subparallel to the glacier bed) and the distribution of source water. The saturated areal fraction of the aquifer is ~ 0.7 in steady state, with unsaturated zones concentrated in the upper basin where meltwater input is low. These zones are conspicuous in Figure 4d as gaps in the modeled groundwater flow field. Groundwater transport attains a maximum beneath the ice margin where subglacial water is being most rapidly evacuated. Such a clear delineation of the glacier boundary in the groundwater flow field is a special consequence of the frozen ice-bed contact.

[28] Simulated profiles of exchange between englacial, subglacial, and groundwater systems are shown together in Figure 4e. Englacial-subglacial exchange $\phi^{e:s}$ is almost exclusively positive (toward the bed), except near the terminus where basal water is expelled back to the surface. The surface runoff system is also fed by groundwater pumping beyond the glacier terminus (not shown). Exchange between the sheet and aquifer $\phi^{s:a}$ is dominated by sheet water loss at the ice boundary. Upstream values of $\phi^{s:a}$ occasionally exhibit reversals in the exchange direction and are not particularly correlated with $\phi^{e:s}$, suggesting that water is redistributed at the glacier bed prior to infiltrating the aquifer.

6. Time-Dependent Simulations: Seasonal Transitions

[29] For many alpine glaciers, spring is associated with the development of a connected and efficient subglacial drainage system [e.g., Seaberg et al., 1988; Hock and

Hooke, 1993] and often accompanied by hydromechanical disturbances (“spring events”) at the glacier bed [e.g., Mair et al., 2001; Kavanaugh and Clarke, 2001]. Prior to spring events, englacial/subglacial water storage augments in response to increasing surface input [e.g., Iken et al., 1983; Anderson et al., 1999], producing high basal water pressure [e.g., Fountain, 1994], glacier uplift, and increased horizontal motion [e.g., Iken et al., 1983]. Elevated solute concentrations in proglacial streams suggest that spring floods can also trigger the release of previously impounded subglacial water [e.g., Anderson et al., 1999]. Transition timing depends on meteorological conditions and snow cover, the latter either related to saturation of the snow/firn aquifer [e.g., Fountain, 1996] or retreat of the snow line itself [Nienow et al., 1998]. Autumn is characterized by collapse of the drainage network and cessation of diurnal water pressure cycling at the bed. The nature of this transition depends on drainage system morphology. We present examples of spring and autumn transitions from the Trapridge Glacier data archive, followed by the results of modeling these two transition types.

6.1. Evidence From Trapridge Glacier

[30] Figure 5a presents an example of summer onset as recorded by two sensors ~ 30 m apart. The P_1 record has been corrected after day 162 when a pressure pulse caused a calibration shift and destroyed sensor P_2 [Kavanaugh and Clarke, 2001]. Diurnal water pressure cycling begins abruptly on day 129, indicating a connection to the glacier surface. Both instruments register mean pressures during connected intervals (those exhibiting diurnal fluctuations) higher than the mean unconnected pressure, reflecting the low capacity of the winter drainage system. Pressure minima are increasingly depressed during days 130–170 (P_1) as the drainage network develops [Kavanaugh and Clarke, 2001]. Nienow et al. [1998] suggest a trio of mechanisms to explain the drainage system development beneath Haut Glacier d’Arolla: melting of basal ice, erosion of unconsolidated sediments, and cavity growth due to enhanced glacier sliding. For Trapridge Glacier, the latter two are probably important, as well as winnowing of fines from the subglacial sediment matrix.

[31] Six records from the 1997 pressure array (Figure 3a) are shown in Figures 5b and 5c to illustrate the autumn transition. Disconnection from the principal drainage network, indicated by disparity between records, occurs rapidly but not simultaneously over the sampled area. In this case, termination of diurnal fluctuations corresponds to the connected-unconnected transition, suggesting that high water fluxes are required to maintain these connections [e.g., Murray and Clarke, 1995; Gordon et al., 1998]. Though typically uncorrelated after the transition, all records show a general increase in water pressure as the drainage system volume decreases.

6.2. Modeling Strategy

[32] We simulate spring and autumn transition types, as illustrated in Figure 5, using 1997 observed air temperature and the reference model parameters in Table 2, except where otherwise noted. Though seasonal signatures in the data arise from combined mechanical and hydraulic pro-

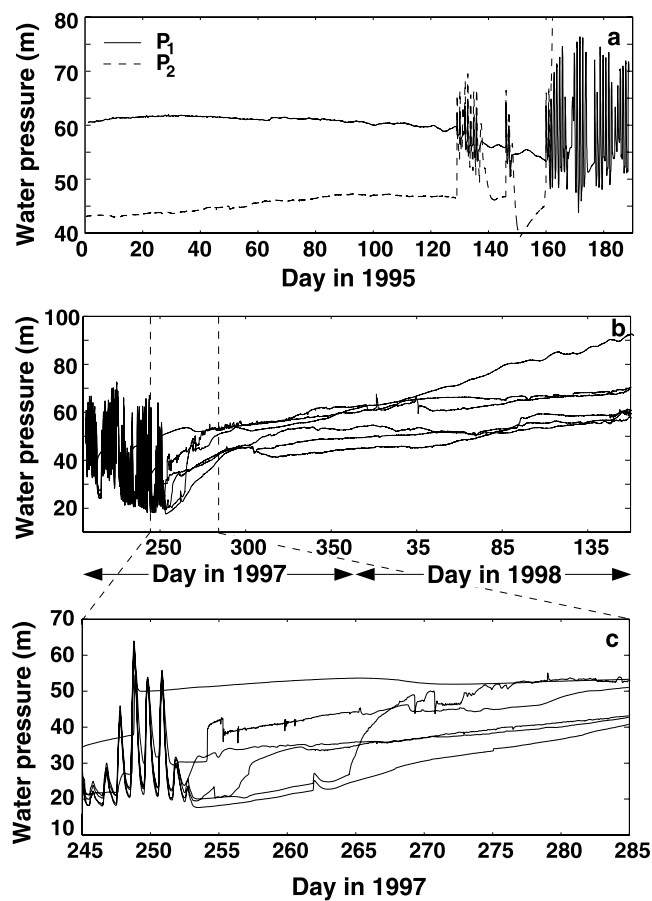


Figure 5. Seasonal transitions recorded by Trapridge Glacier water pressure sensors. (a) Spring 1995. Time axis covers 1 January to 4 July. Day 172 is the summer solstice. (b) Autumn 1997 as recorded by 6 sensors from the array in Figure 3a. Time axis covers 19 July 1997 to 9 April 1998. (b) Detail of transition from 2 September to 12 October 1997.

cesses, we apply the model without additional parameterizations in order to isolate the effects of the water system. For the spring transition, initial snowpack thickness is prescribed in the study area, and its spatial distribution determined by applying a gradient of 0.0082 cm w.e. per meter of elevation gain (estimated for John Evans Glacier, Nunavut, Canada by *Woodward et al.* [1997]).

[33] For both spring and autumn simulations we reduce the minimum subglacial hydraulic conductivity to 10^{-7} m s^{-1} in accord with the estimates of *Fountain* [1994] and *Hubbard et al.* [1995], and shift the transition threshold to very low pressure. This serves to maintain the optimized value of conductivity over a large range of pressures, while permitting a quasi-disconnected hydraulic state at very low water levels.

6.3. Spring: Results and Discussion

6.3.1. Surface Hydrology

[34] Meteorological conditions driving the simulated spring transition are shown in Figures 6a and 6b. Air temperature is recorded by a data logger in the study area

and potential direct solar radiation is computed according to equation (6). Simulated surface melt rates in the study area are plotted in Figure 6c, with snow ablation occupying the first half of the interval and ice ablation the second. The transition from a snow- to ice-covered surface is abrupt in the simulation because no allowance is made for partial snow coverage of individual grid cells.

[35] Evolution of the surface water budget at the test point is shown in Figure 6d. A stepwise decline in snow amount occurs from day 140–160 (20 May to 9 June) until the snowpack is depleted. From day 160–180 (9–29 June) 1.04 m w.e. of ice is ablated, including ~ 0.04 m of superimposed ice. Over the length of the glacier, the maximum predicted thickness of superimposed ice ranges from 0.036 to 0.058 m w.e. At the test point, this maximum is attained in two days, after which liquid water accumulates in the snowpack (Figure 6d). Snowpack saturation requires an additional 12 days, and on day 153 the release of stored water begins contributing to surface runoff in the study area. In the model the maximum depth of stored water is a function of prescribed snow density and snowpack porosity. Figure 6e shows the resulting local rate of water discharge into crevasses ($\phi^{r,e}$).

[36] The simulated spatial evolution of glacier surface variables is illustrated in Figure 6f with time slices that span the spring transition. A snow depth of 0.75 m w.e. is prescribed in the study area for day 140, and the model run is initialized with no superimposed ice or stored water. Due to the strong control of radiation on ablation, the snowpack quickly adjusts from its initial configuration (increasing in thickness steadily upglacier) to one that reflects slope orientation (Figure 6f, row 1, day 154). The persistence of snow along the northern margin is exaggerated in the simulation due to mismatch of fine and coarse DEMs used in the shading calculation.

[37] Modeled superimposed ice (Figure 6f, row 2) covers the entire glacier until its rapid disintegration beginning around day 160. By day 162 its coverage decreases to 68% and by day 166 is down to 12%. The distribution of stored water predicted by the model (Figure 6f, row 3) resembles the snowpack itself, but its maximum migrates headward over time. On day 154, the simulated storage maximum (brightest) covers the study area, while water being released downglacier triggers the development of a surface runoff network (not shown).

6.3.2. Global Water Budget

[38] Figure 7a summarizes the relationship between simulated rates of total surface meltwater production (curve A) and total glacier infiltration (curve B). Peak surface water production prior to day 160 reflects the release of snowpack-stored water, rather than elevated melt rates. Melt rates increase after day 160 in the study area (Figure 6c) and even later over most of the glacier. Figure 7b shows the calculated water capture efficiency of glacier portals over time. This fraction rises abruptly from zero (when the snowpack is unsaturated) to ~ 0.75 over 10 days. Capture fractions this high are typical of temperate glaciers [e.g. *Stenborg*, 1973].

[39] Because of the thermal barrier at the glacier margin, capture efficiency evolution has unusual consequences for the computed runoff hydrograph (Figure 7c). Basin runoff combines all forms of surface water, including artesian

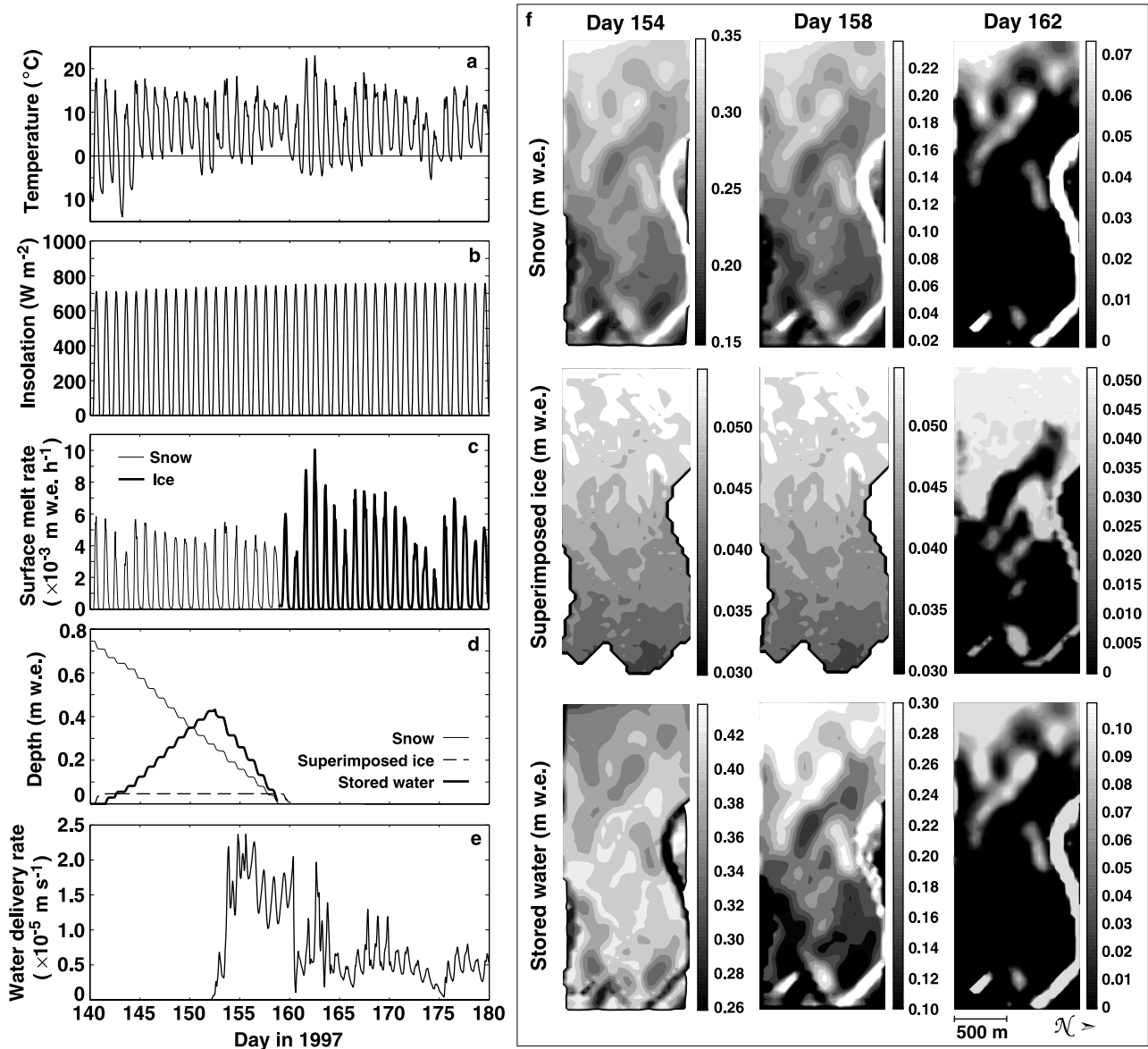


Figure 6. Surface conditions, spring transition, 1997. Results are taken from a crevassed cell in the study area, 2367 m asl (a) Observed air temperature. (b) Potential direct solar radiation calculated by the ablation model. (c) Simulated surface melt rate of snow (fine line) and ice (bold line). (d) Simulated water-equivalent depth of snow (fine line), superimposed ice (dashed line), and water stored in the snowpack (bold line). (e) Simulated rate of water delivery to the glacier interior, $\phi^{r.e}$. (f) Distributions of (top) snow, (middle) superimposed ice, and (bottom) water stored in the snowpack for days 154, 158, and 162.

sources in the glacier forefield. On day 150 in the simulation, a low-level background discharge gives way to diurnal cycling superimposed on a rising baseline. The discharge envelope from day 150 to 160 (30 May to 9 June) is the hydrographic signature of water released from the snowpack. After day 160, the simulated discharge baseline and fluctuation amplitude decrease substantially. In most temperate glacier basins, where subglacial discharge contributes directly to runoff, the hydrographic baseline and fluctuation amplitude increase throughout most of the melt season [e.g., see *Nienow et al.*, 1998, Figure 2; *Mair et al.*, 2001, Figure 5a]. The suggested strengthening of surface-to-bed coupling shown in Figure 7b produces the opposite

effect in our simulations, because some of the water is ultimately discharged through the aquifer rather than as surface runoff.

[40] Modeled surface water input and aquifer discharge are compared in Figure 7d. Discharge exceeds input until the arrival of the first meltwater pulse on day 152. This triggers an increase in englacial/subglacial storage as is commonly reported in the literature [see *Fountain and Walder*, 1998]. Input continues to exceed output for approximately 12 days until meltwater delivery declines toward the end of the flood. On the basis of the evolution of global variables presented in Figure 7, the simulated spring transition occurs over roughly 12–14 days, beginning at the

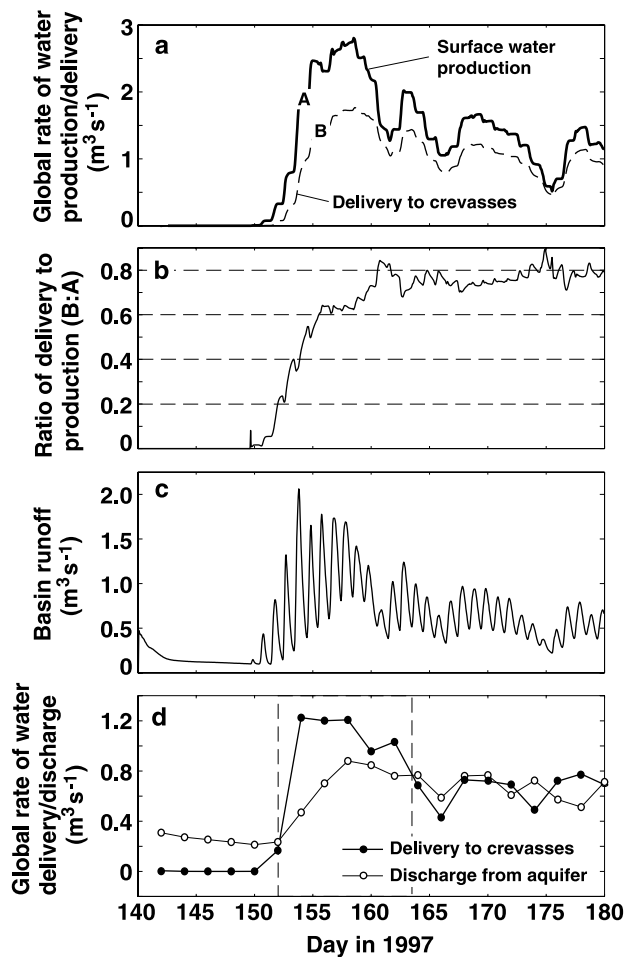


Figure 7. Simulated time series of water production, delivery, runoff, and storage. (a) Global rate of surface water production available for runoff (labeled A) and delivery rate to crevasses (labeled B). Both quantities are shown as 48 hour running averages to eliminate large diurnal variations. (b) Ratio of delivery (B) to production (A). (c) Basin runoff including artesian sources in the glacier forefield. (d) Global water delivery rate to crevasses (solid circles) and total discharge from the aquifer (open circles) sampled every 2 days. Dashed lines bracket the interval of water accumulation associated with the spring flood.

glacier surface on day 150 (Figures 7a–7c) and in the subsurface between days 152 and 154 (Figure 7d).

6.3.3. Subglacial Hydrology

[41] Results highlighting subglacial conditions during the spring transition are summarized in Figure 8. Figure 8a shows the simulated time series of subglacial water pressure in the study area (open circle in Figures 8b–8e). Diurnal cycling commences abruptly after day 153 here, corresponding to snowpack saturation (Figure 6d). The mean water pressure increases for approximately seven days thereafter in response to the pulse of surface water shown in Figure 7a. Water pressure remains above flotation for four days, reaching a maximum of $1.4p_1$. After day 160, the pressure baseline varies between ~ 30 and 60 m (0.55 – $1.1p_1$) with diurnal amplitudes in the range of ~ 10 – 20 m. Amplitudes are generally underpredicted in the simulations

(compare Figure 5) because the physical evolution of the drainage system is not included in the model.

[42] Figures 8b–8e contrast the simulated subglacial conditions in the early (day 154) and middle (day 158) stages of the spring transition in the study area. Widespread

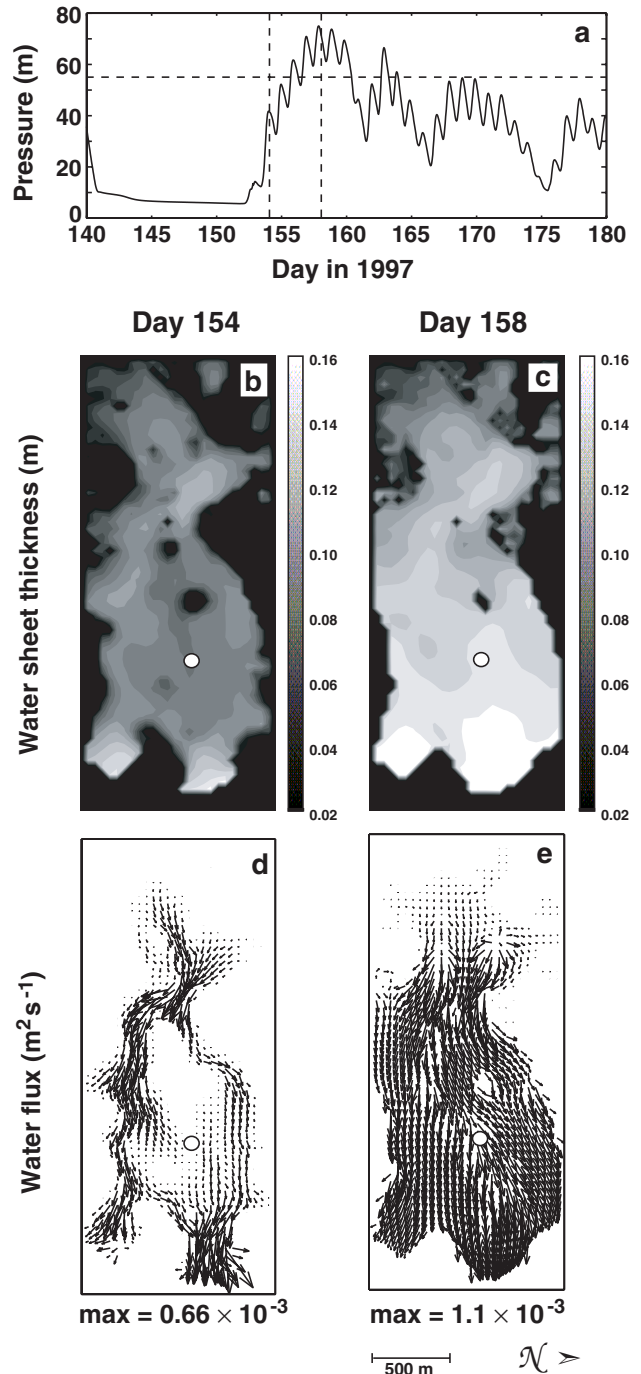


Figure 8. Simulated subglacial conditions: spring, 1997. (a) Water pressure at the test point (open circles in Figures 8b–8e). Horizontal line indicates flotation level (54.6 m). Vertical lines mark days 154 and 158 which illustrate contrasting situations in the drainage system. Distribution of subglacial water on (b) day 154 and (c) day 158. Subglacial flow vectors on (d) day 154 and (e) day 158.

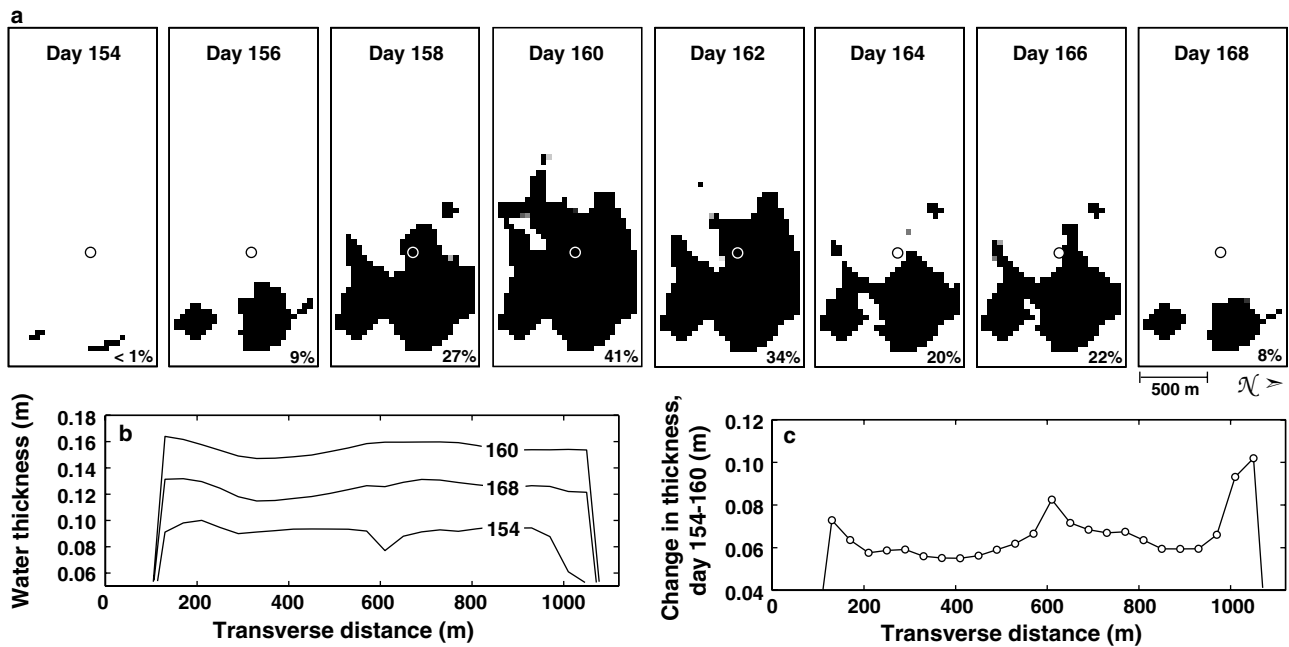


Figure 9. Modeled subglacial signatures of a spring flood. (a) Glacier bed area with water pressure in excess of buoyancy (black) at eight time slices. Percent coverage is noted at the bottom right of each panel. Open circles mark the study area. (b) Transverse profiles of water thickness on days 154, 160, and 168. The profile location intersects the study area near the 600 m mark. (c) Change in subglacially stored water between days 154 and 160. The central maximum coincides with the study area.

subglacial flooding is suggested at this time by a 0.042 m average and 0.18 m maximum change in sheet thickness over the glacier bed from day 154 to 158 (Figures 8b and 8c). *Anderson et al.* [1999] calculated a 0.13 m change in storage over 10 days bracketing a spring flood at Bench Glacier, Alaska. The maximum total subglacial storage predicted here is 0.12 m averaged over the bed, and is relatively insensitive to the initial snowpack thickness: a doubling of the snowpack increases the bed-averaged storage maximum by only 0.02 m.

[43] Subglacial flooding dramatically alters the predicted drainage structure. Water is initially diverted around the study area (Figure 8d) in a network largely controlled by bed topography [Flowers and Clarke, 1999]. By day 158 (Figure 8e) a sheet flood has developed, with a sixfold increase in the mean subglacial water flux compared to day 154. The volume of the active drainage system increases by vertical expansion of the subglacial sheet and by areal growth of the hydraulically connected bed fraction. Early melt season increases in drainage system volume have been documented in the field by *Hock and Hooke* [1993] and *Nienow et al.* [1998].

[44] Figure 9a shows the simulated headward migration and retreat of a high-pressure wave in the basal drainage system. Shaded areas indicate water pressures in excess of buoyancy, which occupy a maximum of 41% of the bed on day 160. This high-pressure tide is reflected in the simulated baseline variations in Figure 8a. Transverse profiles of modeled subglacial water sheet thickness on three different days are plotted in Figure 9b. Storage is augmented along the entire transect from day 154 to day 160 and decreases to an intermediate level by day 168. The computed change in subglacial storage from day 154 to day 160 along this

transect ranges from 0.06 to 0.10 m (Figure 9c). Local maxima are predicted at both margins where drainage is impeded by the thermal barrier. A central maximum of 0.08 m occurs coincident with the study area at 600 m. *Iken et al.* [1983] measured up to 0.60 m of glacier uplift during the early melt season at Unteraargletscher, Switzerland, which they attributed to subglacially stored water. If the Trapridge drainage system were modeled as confined to a smaller fraction of the glacier bed, local changes in subglacially stored water could easily amount to decimeters.

6.3.4. Groundwater Hydrology

[45] Changes in the subglacial system are buffered by the presence of the aquifer. Figure 10a shows longitudinal profiles of simulated subglacial-aquifer exchange $\phi^{s:a}$ (beneath the glacier) and runoff-aquifer exchange $\phi^{r:a}$ (in the forefield) for days 154 and 158. Two key distinctions between these exchange profiles are (1) the general increase in exchange magnitude and (2) the reduced bed fraction over which $\phi^{s:a} < 0$. Both features result from the arrival of surface meltwater at the aquifer interface. Stronger modeled upwelling in the glacier forefield on day 158 (Figure 10a, farthest right) is stimulated by enhanced groundwater transport.

[46] Saturated thickness of the aquifer, as returned by the model (Figures 10b and 10c), responds to the change in source rate between days 154 and 158. Between these snapshots the saturated areal fraction of the aquifer increases from 0.78 to 0.84. This quantity peaks at 0.89 on day 172, 12 days after the maximum extent of the subglacial high-pressure wave (Figure 9a). Figures 10d and 10e show enhanced groundwater transport predicted by the model between days 154 and 158, as well as a

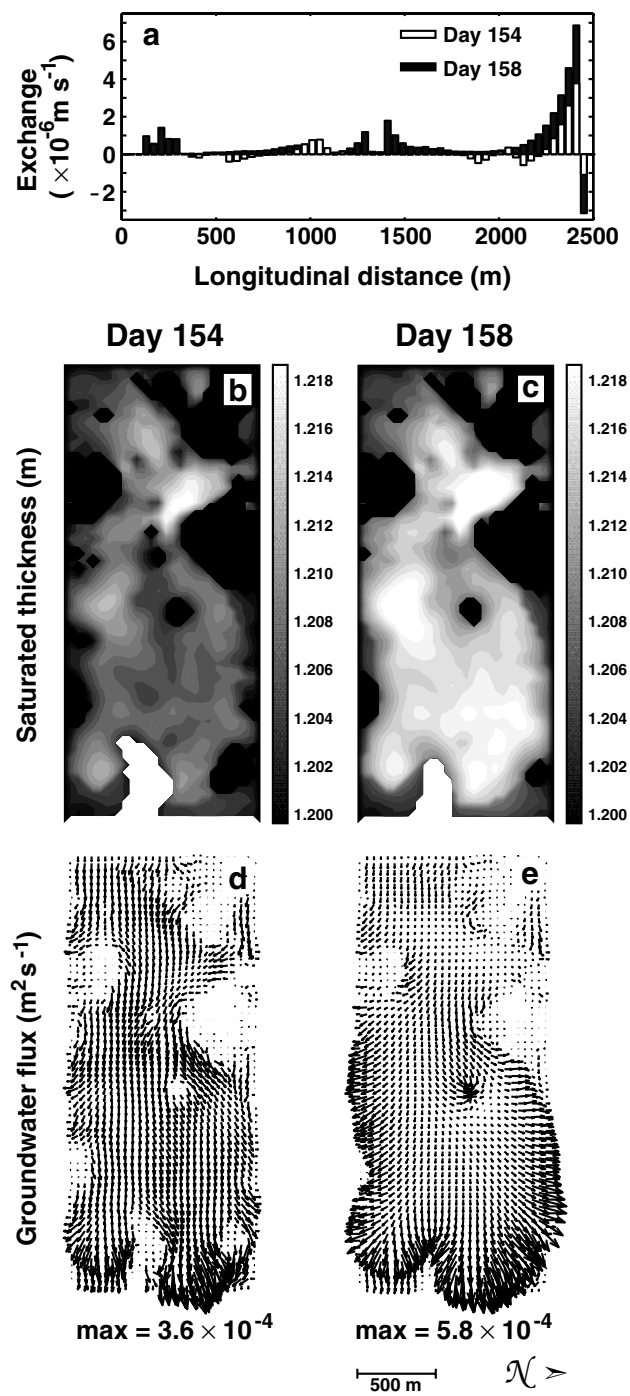


Figure 10. Simulated subsurface conditions: days 154 and 158, 1997. (a) Longitudinal profiles of water exchange with the aquifer ($\phi^{s:a} + \phi^{r:a}$) on days 154 and 158. Positive values correspond to aquifer recharge. Saturated thickness of the aquifer on (b) day 154 and (c) day 158. Groundwater flow vectors on (d) day 154 and (e) 158.

change in flow morphology. Flow enhancement occurs at the glacier margin (Figure 10e) and local perturbations to the flow field are found (e.g., in the center of Figure 10e) where elevated basal source rates recharge unsaturated patches of the aquifer.

6.4. Autumn: Results and Discussion

[47] In this example we consider the period from day 245 to day 285 (2 September to 12 October), 1997 as shown in Figure 5c. To evaluate the influence of precipitation, we conduct two tests referred to as WoP (without precipitation) and WiP (with precipitation).

6.4.1. Surface Hydrology

[48] Figures 11a–11f summarize the surface conditions for both of these tests. According to the observed air temperature record (Figure 11a), there is no surface melt potential in the study area after day 270 (27 September). Calculated insolation (Figure 11b) declines by $\sim 50\%$ from ~ 500 to 250 W m^{-2} during the test interval.

[49] For the WiP simulation, a synthetic precipitation time series is generated by modulating a random series with a cosine function having a 1-year period and minimum in July. The result is filtered so that precipitation only occurs as snow during subfreezing temperatures (Figure 11c). For days 245–285, precipitation totals 0.24 m w.e. in the study area. Snow amount is adjusted for elevation as explained for the spring transition. Because the scheme for superimposed ice formation is based on annual variables, we make the assumption for this test that 60% of melted snowfall refreezes [Reeh, 1991], up to a maximum of ~ 0.04 m w.e.

[50] Simulated surface conditions for WiP at the test point are summarized in Figure 11d. Snow accumulates to a depth of ~ 0.14 m w.e. from day 260 to day 285 (17 September to 12 October) and superimposed ice forms gradually over 10 days from day 260 to day 270. Surface melt rates calculated for WoP and WiP are compared in Figures 11e and 11f. Ice ablation is similar for both until WiP is affected by a permanent snow cover on day 258. A total of 0.24 m w.e. of ice is ablated in the WoP test, while 0.096 m w.e. of snow and 0.12 m w.e. of ice are melted in the WiP test. Total ablation is slightly lower for WiP than WoP (~ 0.22 compared to 0.24 m w.e.) due to the additional energy required for melting snow as compared to ice.

[51] Consequences of snowfall for the simulated runoff hydrograph are illustrated in Figures 11g and 11h. Both records exhibit quasi-sinusoidal oscillations before day 254, followed by a series of exponentially decaying peaks due to low or intermittent melt input. These two signal types represent diffusive responses to periodic and impulse forcing, respectively. Differences in runoff magnitude are small between WoP and WiP, but diurnal variations disappear 14 days earlier and more abruptly in the WiP scenario (Figure 11h). In both cases, the termination of diurnal cycling coincides with the cessation of ice melt. Isolated snowmelt arrivals punctuate the WiP baseline after ice melt ceases on day 257.

6.4.2. Subglacial Hydrology

[52] Figure 12 summarizes spatial changes in the subglacial system through the modeled autumn transition. Simulated distributions of water sheet thickness for days 250 (before) and 285 (after) are compared in Figures 12a and 12b. Between these snapshots, subglacial storage decreases from 0.085 to 0.056 m averaged over the bed. This loss in storage is concentrated in the upper basin, at the glacier terminus, and in isolated interior patches. Modeled water fluxes in Figures 12c and 12d suggest a general deterioration of the drainage system, which is pronounced in the study area.

[53] Profiles of simulated water exchange with the aquifer (Figure 12e) show marked differences between days 250

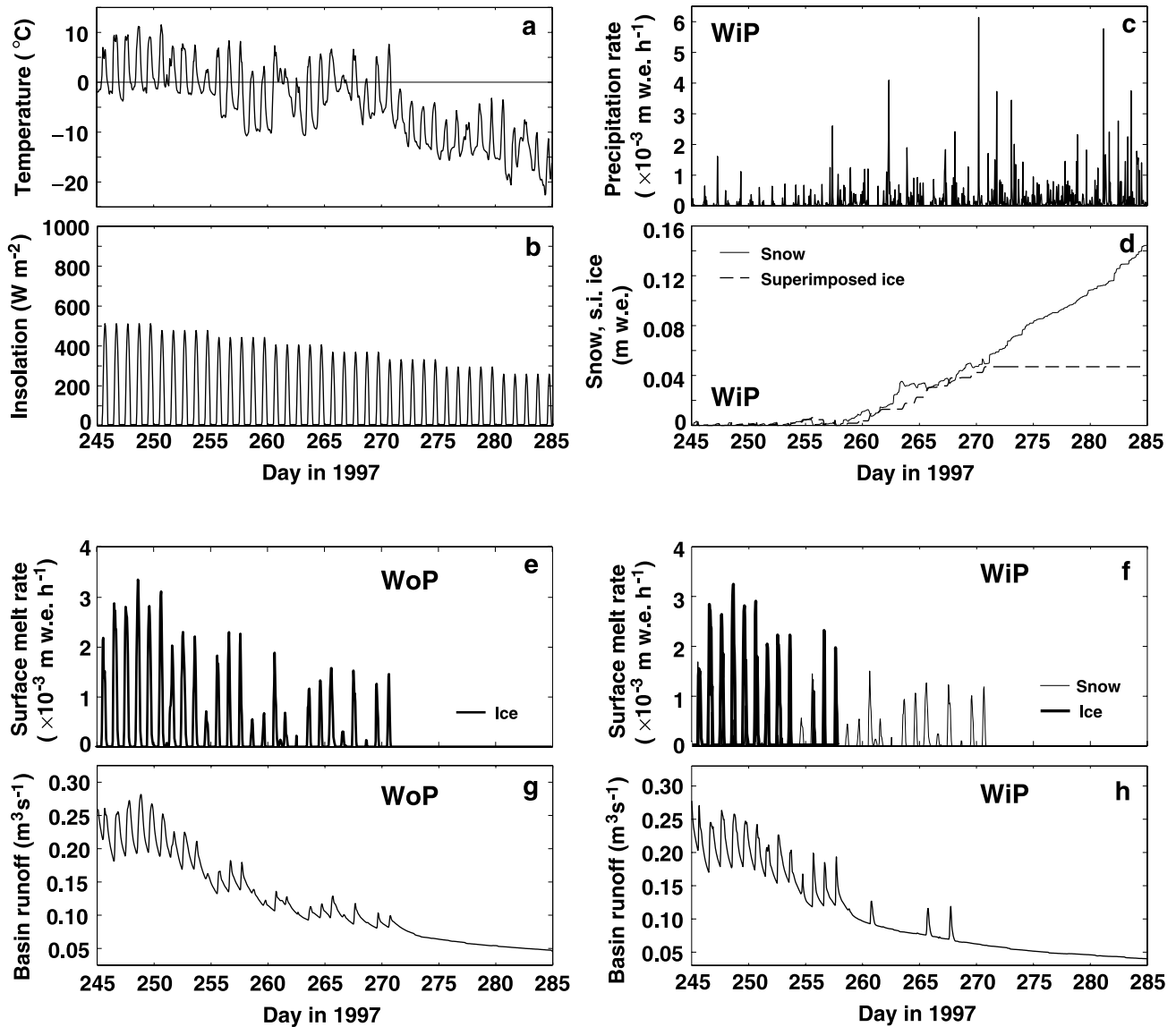


Figure 11. Autumn transition, 1997: possible surface conditions with and without precipitation (WiP and WoP, respectively). Figures 11a and 11b apply equally to WiP and WoP. Figures 11c and 11d apply only to WiP. Time series shown in Figures 11a–11f are taken from a crevassed cell in the study area. (a) Observed air temperature. (b) Potential direct solar radiation as calculated by the ablation model. (c) Synthetically generated precipitation rate for WiP. (d) Simulated water-equivalent depth of snow and superimposed ice for WiP. (e) Simulated melt rate of ice for WoP. (f) Simulated melt rate of snow (fine line) and ice (bold line) for WiP. (g) Basin runoff for WoP. (h) Basin runoff for WiP.

and 285. Prior to the transition (day 250), exchange along this profile is dominated by sheet water infiltration at the glacier terminus, accompanied by forefield upwelling. By day 285, the exchange maximum has retreated upglacier and been reduced by a factor of 4. According to these results, the saturated areal fraction of the aquifer decreases from 0.84 to 0.70 between day 250 and day 285 (7 September and 12 October).

7. Summary and Conclusions

[54] This study constitutes the first basin-scale modeling of Trapridge Glacier and employs the first glaciohydraulic model to couple surface, englacial, subglacial, and ground-

water drainage. We adopt a temperature index ablation routine that incorporates spatially variable radiation to calculate the surface forcing, and exploit subglacial water pressure records to derive a reference model. A crude characterization of the drainage structure is interpreted from the simulated steady state, and time-dependent tests reveal the spatial and temporal signatures of seasonal transitions in a manner consistent with available field data.

7.1. Seasonal Transitions

7.1.1. Spring

[55] The timing of the spring transition depends on initial snow depth, the propensity for superimposed ice formation, and weather. With our best parameter estimates, the ablation

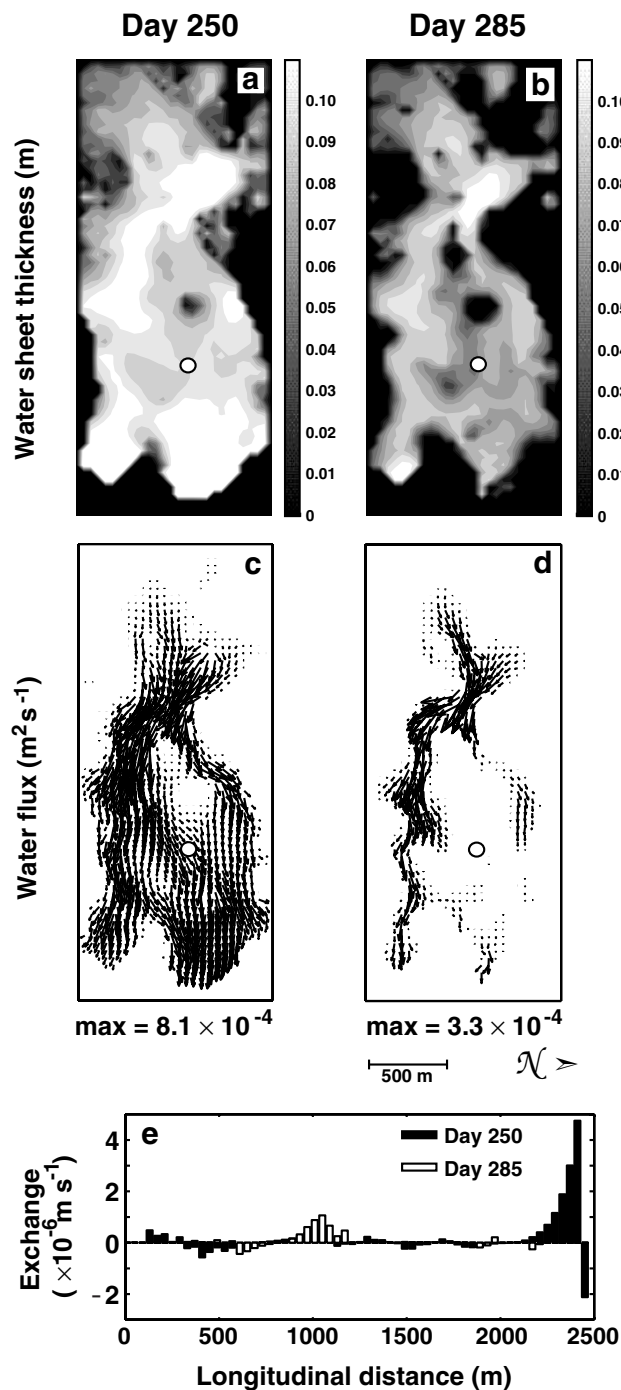


Figure 12. Simulated subglacial conditions (WoP): days 250 and 285, 1997. Results from WoP and WiP are similar. Distribution of subglacial water on (a) day 250 and (b) day 285. Subglacial flow vectors on (c) day 250 and day (d) 285. (e) Longitudinal profiles of water exchange with the aquifer ($\phi^{s:a} + \phi^{r:a}$) on days 250 and 285. Positive values correspond to aquifer recharge.

model predicts rapid disintegration of the snowpack: 0.74 m w.e. over 20 days in the study area with 1997 meteorology. Spatial patterns of ablation appear more sensitive to slope aspect than to elevation. Simulated surface-stored water accumulates over 12 days to a maximum of 0.45 m in the

same area. This value depends linearly on the prescribed porosity and initial depth of snow, and varies inversely with snow density. The zone of maximum water storage, as predicted by the surface hydrology model, migrates steadily upglacier and a supraglacial runoff network develops in its wake.

[56] In the spring simulation, diurnal water pressure variations at the glacier bed begin approximately 13 days after the onset of surface melting. In a simulation initialized with 1.0 rather than 0.75 m w.e. of snow, subglacial diurnal fluctuations are postponed by only three days. With 1.5 m w.e. initial snow, surface water first reaches the bed after 24 days, but strong fluctuations do not begin for another four days. When the snowpack is saturated, a unit of energy applied to ablation produces a disproportionate quantity of runoff due to in situ water storage. Therefore this period in the simulation has the characteristics of a spring flood. Crevasses capture $\sim 70\%$ of modeled supraglacial runoff within 10 days of the onset of water production. During this time, predicted basin runoff reaches its maximum and water begins accumulating in the aquifer. Simulated groundwater discharge eventually increases and surface runoff declines to a baseline value of $\sim 0.7 \text{ m}^3 \text{ s}^{-1}$.

[57] Flooding of the glacier bed causes an average change in modeled subglacial storage of 0.042 m, with a value almost double that in the study area. Maximum total subglacial storage is predicted to be 0.12 m averaged over the bed. Results show a wave of high subglacial water pressure moving headward from the terminus for the first 6 days of the flood and covering most of the ablation zone at its maximum. High pressures then subside after the initial pulse of water passes through and is discharged to the aquifer.

[58] The modeled timing and duration of the spring transition represent earliest or minimum estimates. The presence of firm may retard, if not prevent, summer subglacial signals in certain sectors of the glacier. Moreover, the presence of meltwater on the glacier surface does not guarantee that an internal drainage system will develop. There have been years in which no discernible basal drainage system has developed at Trapridge Glacier.

7.1.2. Autumn

[59] Simulations of the autumn transition suggest that late season snowfalls can prematurely terminate diurnal glacier discharge cycles. In the tests presented here, the additional energy required to produce runoff from snow rather than ice becomes unavailable 14 days before surface melting stops altogether in the study area. As a consequence, simulated water delivery to the glacier is interrupted even though snow continues to ablate at the surface. As confirmation, the predicted runoff hydrograph shows several late season meltwater pulses that are not present beneath most of the glacier.

[60] With or without autumn snowfall included in the model, the simulated decrease in water flux to the bed allows what can be interpreted as a deterioration of basal hydraulic connectivity. During this time, results show a release of water stored within and beneath the glacier. Simulated aquifer saturation decreases concomitantly, drawing sheet water away from storage reservoirs in the upper basin. Vigorous water exchange, predicted near the glacier terminus during most of the melt season, finally shuts down

along with modeled artesian discharge in the glacier forefield.

[61] This simple analysis suggests that even a modest amount of autumn snowfall can send the system into a dormant state by tying up ablative energy. This result is not generally applicable, as other studies find evidence for connected, low-pressure hydrology persisting beyond the melt season [e.g., Harbor *et al.*, 1997]. However, this probably represents a difference stemming from temperate versus nontemperate ice. In the former case, drainage system collapse may be tuned to the gradual closure of cylindrical tunnels by ice deformation. The drainage system beneath a nontemperate glacier more likely comprises horizontal slot-like passages, which can be clamped off much more rapidly than ice-walled conduits.

7.2. Trapridge Glacier Hydrology

[62] Trapridge Glacier hydrology is strongly affected by the frozen glacier margin. The combination of a transmissive substrate and such a thermal barrier results in simulated subglacial water pressures in excess of flotation at the terminus, and predicted groundwater upwelling in the forefield during the melt season. The frozen perimeter is probably a key deterrent to conduit formation beneath Trapridge, in addition to relatively low source rates and the presence of transmissive strata underlying the till. Mid melt season simulations (days ~ 160 – 240) show rates of total surface water production less than $2 \text{ m}^3 \text{ s}^{-1}$, and delivery rates to the glacier body generally less than $1.5 \text{ m}^3 \text{ s}^{-1}$. The conduit-forming potential of this system is further reduced by its comparatively distributed injection of meltwater into the glacier via numerous crevasses, rather than through a small number of moulins. Simulated basin surface runoff is typically on the order of $1 \text{ m}^3 \text{ s}^{-1}$, with the remainder of water escaping through the subsurface.

[63] Realistic simulations of instrument records require high values of subglacial and subsurface hydraulic conductivity to account for flow through the connected fraction of the drainage network. Even so, our best estimates for these parameters fall within the bounds determined from field studies, with $K_{\text{max}}^s = 5 \times 10^{-2} \text{ m s}^{-1}$ (subglacial sheet), $K^t = 5 \times 10^{-8} \text{ m s}^{-1}$ (till cap), and $K^a = 4 \times 10^{-4} \text{ m s}^{-1}$ (aquifer). Deviations from these preferred values produce a markedly poorer fit to the observations, most notably in the basal water pressure baseline. However, spatial distributions of hydraulic variables are relatively robust to modest (within a factor of 2) parameter adjustments, owing to the dominant influence of glacier geometry. Conspicuous changes in the modeled hydrology occur when conductivities are low enough to cause water to back up into the englacial system, sometimes resulting in artesian fountains near the glacier terminus. A full parameter sensitivity study is presented by Flowers [2000].

[64] Given the reference model parameter values, it is plausible that the aquifer can evacuate ordinary quantities of subglacial water during the melt season. Crude mean estimates of basal water velocity from summer simulations suggest that travel times between the study area and terminus are on the order of 2–3 days through the subglacial horizon and 100–150 days through the aquifer. The actual travel time for a parcel of water depends on the partitioning of its path between these two layers. In the

ablation area, simulated horizontal fluxes are much greater than leakage fluxes to the aquifer, which partially accounts for high subglacial water pressures predicted at the terminus. In most test simulations, the areal extent of aquifer saturation is 70–90%, with unsaturated regions concentrated in the upper basin and beyond the glacier margin. Supersaturation persists beneath the ablation zone and in the vicinity of the ice margin in these simulations, positioning the drainage system on the edge of its capacity. Hydro-mechanical events therefore seem likely to occur with small perturbations to the ordinary water supply.

[65] Our results suggest that the instrument study area is favorably situated to capture such glaciohydraulic phenomena. It is positioned just downstream from what may be a hydraulic pinning point, and proximal upstream crevasses tap into a large catchment originating in the upper basin. Spring and autumn simulations suggest more dramatic changes in both water flux and storage in the study area compared to its immediate surroundings.

[66] The capacity of Trapridge Glacier for water storage remains an open question. Spatially uniform parameter estimates produce a consistent storage hierarchy in the model, with 1.5 – $3.5 \times 10^6 \text{ m}^3$ of water in the aquifer, 1 – $3 \times 10^5 \text{ m}^3$ at the glacier bed, and 4 – $40 \times 10^2 \text{ m}^3$ in englacial voids. Spatial variability in aquifer thickness is completely unconstrained, so groundwater storage may be misrepresented by an order of magnitude. Errors in the subglacial estimate may tend to cancel out: storage may be overestimated by assuming spatial continuity of the sediment layer, but underestimated by neglecting storage in subglacial cavities. Storage capacity may also be much lower if the glacier bed has a substantial frozen fraction.

[67] Englacial storage volume has effectively been tuned to produce recognizable subglacial signals. Only surface crevasses were used for this purpose, so water storage in basal crevasses has not been included. While we are uncertain as to the existence of basal crevasses at Trapridge, they provide a conceptual solution to the problem of impounding abnormal amounts of water in preparation for a surge. Humphrey and Raymond [1994] calculated the volume of stored water at Variegated Glacier during its 1982–1983 surge to be greater than 1 m averaged over the bed. Furthermore, they determined that much of it was stored englacially. Were Trapridge to have 1% of its ice volume (within the area covered by the DEM) dedicated to englacial storage, this would amount to $\sim 1.7 \times 10^6 \text{ m}^3$ of water, or 0.7 m averaged over the glacier bed.

[68] **Acknowledgments.** Members of the Trapridge Glacier field crew, Dave Hildes and Jeff Kavanaugh in particular, are gratefully acknowledged for collecting the data presented here. Regine Hock computed the digital slope and aspect models and provided generous support along with her software. Thorough reviews by Bryn Hubbard and Peter Nienow led to marked improvements in the scientific and technical quality of the manuscript. Many helpful comments were provided by Tim Creyts in a preliminary review. This research was funded by the Natural Sciences and Engineering Research Council of Canada and supported by the Arctic Institute of North America. We thank our friends at the Kluane Lake Research Station base for their logistical support.

References

- Alley, R. B., Water-pressure coupling of sliding and bed deformation, I, Water system, *J. Glaciol.*, 35, 108–139, 1989.
- Anderson, S. P., K. M. H. Fernald, R. S. Anderson, and N. F. Humphrey, Physical and chemical characterization of a spring flood event, Bench

- Glacier, Alaska: Evidence for water storage, *J. Glaciol.*, 45, 177–189, 1999.
- Arnold, N. S., K. S. Richards, I. C. Willis, and M. J. Sharp, Initial results from a semi-distributed, physically based model of glacier hydrology, *Hydrol. Proc.*, 12, 191–220, 1998.
- Bindschadler, R. A., The importance of pressurized subglacial water in separation and sliding at the glacier bed, *J. Glaciol.*, 29, 3–19, 1983.
- Björnsson, H., Hydrological characteristics of the drainage system beneath a surging glacier, *Nature*, 395, 771–774, 1998.
- Blake, E. W., The deforming bed beneath a surge-type glacier: measurements of mechanical and electrical properties, Ph.D. thesis, 179 pp., Univ. of B.C., Vancouver, Canada, 1992.
- Blake, E. W., U. H. Fischer, and G. K. C. Clarke, Direct measurement of sliding at the glacier bed, *J. Glaciol.*, 40, 595–599, 1994.
- Clarke, G. K. C., Subglacial till: A physical framework for its properties and processes, *J. Geophys. Res.*, 92, 9023–9036, 1987.
- Clarke, G. K. C., and E. W. Blake, Geometric and thermal evolution of a surge-type glacier in its quiescent state: Trapridge Glacier, Yukon Territory, Canada, 1969–89, *J. Glaciol.*, 37, 158–169, 1991.
- Fischer, U. H., and G. K. C. Clarke, Ploughing of subglacial sediment, *J. Glaciol.*, 40, 97–106, 1994.
- Fischer, U. H., and G. K. C. Clarke, Stick-slip sliding behaviour at the base of a glacier, *Ann. Glaciol.*, 24, 390–396, 1997.
- Flowers, G. E., A multicomponent coupled model of glacier hydrology, Ph.D. thesis, 265 pp., Univ. of B.C., Vancouver, Canada, 2000.
- Flowers, G. E., and G. K. C. Clarke, Surface and bed topography of Trapridge Glacier, Yukon Territory, Canada: Digital elevation models and derived hydraulic geometry, *J. Glaciol.*, 45, 165–174, 1999.
- Flowers, G. E., and G. K. C. Clarke, An integrated modelling approach to understanding subglacial hydraulic release events, *Ann. Glaciol.*, 31, 222–228, 2000.
- Flowers, G. E., and G. K. C. Clarke, A multicomponent coupled model of glacier hydrology, 1, Theory and synthetic examples, *J. Geophys. Res.*, 107(BX), XXXX, doi:10.1029/2001JB001122, in press, 2002.
- Fountain, A. G., Borehole water-level variations and implications for the subglacial hydraulics of South Cascade Glacier, Washington State, U.S.A., *J. Glaciol.*, 40, 293–304, 1994.
- Fountain, A. G., Effect of snow and firn hydrology on the physical and chemical characteristics of glacial runoff, *Hydrol. Proc.*, 10, 509–521, 1996.
- Fountain, A. G., and J. S. Walder, Water flow through temperate glaciers, *Rev. Geophys.*, 36, 299–328, 1998.
- Fowler, A. C., Sliding with cavity formation, *J. Glaciol.*, 33, 255–267, 1987.
- Freeze, A., and J. A. Cherry, *Groundwater*, 1st ed., 604 pp., Prentice-Hall, Old Tappan, N. J., 1979.
- Fröhlich, C., Changes of total solar irradiance, in *Interactions Between Global Climate Subsystems: The Legacy of Hann*, *Geophys. Monogr. Ser.*, vol. 75, edited by G. A. McBean and M. Hantel, pp. 123–129, AGU, Washington, D. C., 1993.
- Garnier, B., and A. Ohmura, A method of calculating the direct short-wave radiation income on slopes, *J. Appl. Meteorol.*, 7, 796–800, 1968.
- Gordon, S., M. Sharp, B. Hubbard, C. C. Smart, B. Ketterling, and I. C. Willis, Seasonal reorganization of subglacial drainage inferred from measurements in boreholes, *Hydrol. Proc.*, 12, 105–133, 1998.
- Harbor, J., M. Sharp, L. Copeland, B. Hubbard, P. Nienow, and D. Mair, Influence of subglacial drainage conditions on the velocity distribution within a glacier cross section, *Geology*, 25, 739–742, 1997.
- Hock, R., A distributed temperature-index ice- and snowmelt model including potential direct solar radiation, *J. Glaciol.*, 45, 101–111, 1999.
- Hock, R., and R. LeB. Hooke, Evolution of the internal drainage system in the lower part of the ablation area of Storglaciären, Sweden, *Geol. Soc. Am. Bull.*, 105, 537–546, 1993.
- Hubbard, B. P., M. J. Sharp, I. C. Willis, M. K. Nielsen, and C. C. Smart, Borehole water-level variations and the structure of the subglacial hydrological system of Haut Glacier d’Arolla, Valais, Switzerland, *J. Glaciol.*, 41, 572–583, 1995.
- Humphrey, N. F., and C. F. Raymond, Hydrology, erosion and sediment production in a surging glacier: Variegated Glacier, Alaska, 1982–83, *J. Glaciol.*, 40, 539–552, 1994.
- Iken, A., The effect of the subglacial water pressure on the sliding velocity of a glacier in an idealized numerical model, *J. Glaciol.*, 27, 407–421, 1981.
- Iken, A., and R. A. Bindschadler, Combined measurements of subglacial water pressure and surface velocity of Findelengletscher, Switzerland: Conclusion about drainage system and sliding mechanism, *J. Glaciol.*, 32, 101–119, 1986.
- Iken, A., H. Röthlisberger, A. Flotron, and W. Haeblerli, The uplift of Unteraargletscher at the beginning of the melt season—A consequence of water storage at the bed?, *J. Glaciol.*, 29, 28–47, 1983.
- Kamb, B., Sliding motion of glaciers: theory and observation, *Rev. Geophys.*, 8, 673–728, 1970.
- Kavanaugh, J. L., Hydromechanical behaviour of a surge-type glacier: Trapridge Glacier, Yukon Territory, Canada, Ph.D. thesis, 107 pp., Univ. of B. C., Vancouver, Canada, 2000.
- Kavanaugh, J. L., and G. K. C. Clarke, Abrupt glacier motion and reorganization of basal shear stress following the establishment of a connected drainage system, *J. Glaciol.*, 47, 472–480, 2001.
- Mair, D., P. Nienow, I. Willis, and M. Sharp, Spatial patterns of glacier dynamics during a high velocity event: Haut Glacier d’Arolla, Switzerland, *J. Glaciol.*, 47, 9–20, 2001.
- Murray, T., and G. K. C. Clarke, Black-box modeling of the subglacial water system, *J. Geophys. Res.*, 100, 10,219–10,230, 1995.
- Nienow, P. W., M. Sharp, and I. C. Willis, Seasonal changes in the morphology of the subglacial drainage system, Haut Glacier d’Arolla, Switzerland, *Earth Surf. Processes Landforms*, 23, 823–845, 1998.
- Reeh, N., Parameterization of melt rate and surface temperature on the Greenland Ice Sheet, *Polarforschung*, 59, 113–128, 1991.
- Seaberg, S. Z., J. Z. Seaberg, R. LeB. Hooke, and D. W. Wiberg, Character of the englacial and subglacial drainage system in the lower part of the ablation area of Storglaciären, Sweden, as revealed by dye-trace studies, *J. Glaciol.*, 34, 217–227, 1988.
- Stenborg, T., Some viewpoints on the internal drainage of glaciers, in *Hydrology of Glaciers*, IASH Publ., 95, 117–129, 1973.
- Stone, D. B., Characterization of the basal hydraulic system of a surge-type glacier: Trapridge Glacier, 1989–92, Ph.D. thesis, 187 pp., Univ. of B. C., Vancouver, Canada, 1993.
- Stone, D. B., and G. K. C. Clarke, In situ measurements of basal water quality and pressure as an indicator of the character of subglacial drainage systems, *Hydrol. Proc.*, 10, 615–628, 1996.
- Ward, W. H., and S. Orvig, The glaciological studies of the Baffin Island Expedition, 1950, part IV, The heat exchange at the surface of the Barnes Ice Cap during the ablation period, *J. Glaciol.*, 2, 158–168, 1953.
- Woodward, J., M. Sharp, and A. Arendt, The influence of superimposed-ice formation on the sensitivity of glacier mass balance to climate change, *Ann. Glaciol.*, 24, 186–190, 1997.

G. K. C. Clarke and G. E. Flowers, Department of Earth and Ocean Sciences, University of British Columbia, 2219 Main Mall, Vancouver, B.C., Canada V6T 1Z4. (clarke@geop.ubc.ca; flowers@geop.ubc.ca)